Mon. Not. R. Astron. Soc. **000**, 1–13 (2015) Printed 17 August 2016 (MN LaTeX style file v2.2)

The effects of bar-spiral coupling on stellar kinematics in the Galaxy

Giacomo Monari[1⋆], Benoit Famaey[1], Arnaud Siebert[1], Robert J.J. Grand[23], Daisuke Kawata[4], Christian Boily[1]

[1] *Observatoire astronomique de Strasbourg, Université de Strasbourg, CNRS, UMR 7550, 11 rue de l'Université, F-67000 Strasbourg, France*
[2] *Heidelberger Institut für Theoretische Studien, Schloss-Wolfsbrunnenweg 35, 69118 Heidelberg, Germany*
[3] *Zentrum für Astronomie der Universität Heidelberg, Astronomisches Recheninstitut, Mönchhofstr. 12-14, 69120 Heidelberg, Germany*
[4] *Mullard Space Science Laboratory, University College London, Holmbury St. Mary, Dorking, Surrey, RH5 6NT, United Kingdom*

arXiv:1606.06785v2 [astro-ph.GA] 16 Aug 2016

17 August 2016

ABSTRACT

We investigate models of the Milky Way disc taking into account simultaneously the bar and a two-armed quasi-static spiral pattern. Away from major resonance overlaps, the mean stellar radial motions in the plane are essentially a linear superposition of the isolated effects of the bar and spirals. Thus, provided the bar is strong enough, even in the presence of spiral arms, these mean radial motions are predominantly affected by the Galactic bar for large scale velocity fluctuations. This is evident when comparing the peculiar line-of-sight velocity power spectrum of our coupled models with bar-only models. However, we show how forthcoming spectroscopic surveys could disentangle bar-only non-axisymmetric models of the Galaxy from models in which spiral arms have a significant amplitude. We also point out that overlaps of low-order resonances are sufficient to enhance stellar churning within the disc, even when the spirals amplitude is kept constant. Nevertheless, for churning to be truly non-local, stronger or (more likely) transient amplitudes would be needed: otherwise the disc is actually mostly unaffected by churning in the present models. Finally, regarding vertical breathing modes, the combined effect of the bar and spirals on vertical motions is a clear non-linear superposition of the isolated effects of both components, significantly superseding the linear superposition of modes produced by each perturber separately, thereby providing an additional effect to consider when analysing the observed breathing mode of the Galactic disc in the extended Solar neighbourhood.

Key words: Galaxy: kinematics and dynamics – Galaxy: solar neighborhood – Galaxy: structure – Galaxy: evolution – galaxies: spiral

1 INTRODUCTION

The Milky Way disc has long been known to possess non-axisymmetries, essentially in the form of a central bar and spiral arms. But our detailed understanding of the nature and of the dynamical effects of these structures is still in its infancy. These structures are important because they are significant drivers of dynamics and evolution of the Galaxy, through effects such as in-plane heating and radial migration (Sellwood & Binney 2002; Minchev & Famaey 2010).

The nature and origin of spiral arms is still a matter of debate, and interpretations of spirals in self-consistent numerical simulations range from very transient co-rotating structures (dynamic spirals) which wind up and disappear over time (e.g. Grand et al. 2012; Baba et al. 2013; Grand et al. 2015a) to multiple long-lived ($\sim$ 10 galaxy rotations) modes (e.g. Minchev et al. 2012; Quillen et al. 2011; D'Onghia et al. 2013; Sellwood & Carlberg 2014). In the latter case, even though such modes do not appear to be strictly static as in the classical density wave picture, they are nevertheless genuine standing wave oscillations with fixed shape and pattern speed. In principle the response of stars and gas to these waves away from the main resonances can be computed from linear perturbation theory (Lin & Shu 1964, 1966; Monari et al. 2016, hereafter M16) and can be simply added to each other if there is no nonlinear density growth when the modes overlap each other. Hence it is interesting to consider the response to single modes in test-particle simulations to get an insight of the effects of such modes on the kinematics of stellar populations of the Galactic disc. Un-

⋆ giacomo.monari@astro.unistra.fr

like Grand et al. (2015a), we will consider here non-varying amplitudes only. Note that our models will also differ from those by not taking self-gravity into account, but have the advantage of controlling the strength of the perturbation. Such test-particle simulations can be very useful as benchmarks for analytical models such as those developed in M16. Such simulations have also allowed to demonstrate in the past how local velocity-space substructures made of stars of different ages and chemical compositions, known as moving groups in the Solar neighbourhood (e.g. Chereul et al. 1998; Dehnen 1998; Famaey et al. 2005), are typical responses to a given spiral mode near its resonances (e.g. Quillen & Minchev 2005; Pompéia et al. 2011; Antoja et al. 2011). The outer Lindblad resonance (OLR) from the central bar is generally acknowledged to play a similar role in explaining the kinematic group known as the Hercules stream (e.g. Dehnen 2000; Monari et al. 2013). The role of the bar in driving or sustaining spiral arms is on the other hand still unclear. While there are clear mechanisms for generating bar-driven spiral arms sharing the same pattern speed as the bar (e.g. Romero-Gómez et al. 2007; Sormani et al. 2015), there is also evidence that the Milky Way central bar and the main spiral pattern at the Solar position do not share the same pattern speed. However, even the pattern speed of the Milky Way bar itself is still subject to debate, as recent results from Wegg et al. (2015) and Portail et al. (2015) argue for a much smaller pattern speed than previously estimated. This would nevertheless make it difficult to explain the presence of the Hercules stream in the Solar vicinity (Monari et al. in preparation).

The probable combined presence of a bar and spiral arms having *different* pattern speeds in our Galaxy thus makes it of utmost importance to understand how their combination affects stellar kinematics. Away from major resonances, as stated above, it is a priori expected that the average in-plane motions are a linear superposition of both. It is nevertheless important to understand the behavior at resonances too, both in terms of radial migration of stars in the disc[1], and in view of recent observations of non-zero mean stellar radial motions within the disc. Indeed, using line-of-sight velocities of 213713 stars from the RAVE survey, Siebert et al. (2011) found a Galactocentric radial velocity gradient of $\partial V_R/\partial R \simeq -4\,\mathrm{km\,s^{-1}\,kpc^{-1}}$ in the extended Solar neighbourhood. Siebert et al. (2012) found that such a gradient is consistent with the effect of a $m = 2$ quasi-static spiral density wave, derived by Lin & Shu (1964), although M16 showed that the reduction factor is different in 3D. Monari et al. (2014) found the gradient consistent with the effects of the Galactic bar, according to test-particle simulations. Line-of-sight velocity fluctuations have subsequently been detected on larger scales with red clump stars from the APOGEE survey (Bovy et al. 2015), and we have then shown how the peculiar velocity power spectrum of a N-body simulation with a strong central bar and transient, co-rotating spiral arms fits very well the observed power spectrum, while a quasi-stationary density wave spiral model without a bar does not (Grand et al. 2015a). Hereafter, we will now check the peculiar velocity power spectrum in a simulation coupling the effects of both a bar and a quasi-static spiral mode.

Not only non-zero mean radial motions have been found with recent spectroscopic surveys, but also non-zero mean vertical motions (Widrow et al. 2012; Williams et al. 2013; Carlin et al. 2013), which have amplitudes $\lesssim 5$ km s^{-1} near the Galactic plane, but can reach ~ 15 km s^{-1} at large heights (~ 1.5 kpc), with a gradient of the order of $\partial|V_z|/\partial z \sim 10^{-2}$ km s^{-1} pc^{-1} at the Solar position. These typically consist in 'breathing modes' or 'bending modes' of the disc. Breathing modes (bending modes) are vertical modes with an odd (even) parity in the vertical velocity field and even (odd) parity in the density distribution of the stars. It was shown that any internal non-axisymmetric perturbations, such as the bar and spiral arms, naturally cause breathing modes (Faure et al. 2014; Monari et al. 2015, 2016, hereafter F14, M15, and M16). Nevertheless, it appears that the mean vertical motions induced by the bar in the Solar vicinity are much smaller than the observed ones (M15). Those linked to spiral arms are more important (F14, M16), due to a more rapid radial variation of their potential, but still need unrealistically large amplitudes to reproduce the observed mean motions. Hence, we investigate here the effects of coupled bar and spirals in test-particle simulations, to test whether the vertical motions arise from a simple linear addition of the isolated effects of both, as it is expected to be the case for in-plane motions.

In Section 2, we describe the set-up of our test-particle simulations with a bar, a fiducial spiral pattern (30 per cent density contrast) and strong spiral pattern (60 per cent density contrast), and simulations taking into account both the bar and spirals simultaneously. We analyze the power spectra of peculiar line-of-sight velocities in Section 3. We then analyze the detailed velocity field of each simulation in Section 4, the effect of the coupling and resonance overlaps on disc churning in Section 5, and make predictions for forthcoming spectroscopic surveys in Section 6. We conclude in Section 7.

2 SET-UP OF SIMULATIONS

In the following test-particle simulations we integrate forward in time the equations of motion of massless particles (representing the stars of the Milky Way disc) moving in a gravitational potential (representing the potential of the Milky Way and its non-axisymmetries), uninfluenced by the particles themselves.

2.1 Potential

The potential that we use to represent the gravitational field of the Milky Way is composed of an axysimmetric part and (i) of a bar, or (ii) of a two-armed spiral pattern, or (iii) of both. In the following, we use the Galactocentric cylindrical coordinates (R, ϕ, z), and velocities $(v_R, v_\phi, v_z) \equiv \left(\dot{R}, R\dot{\phi}, \dot{z}\right)$.

The axisymmetric part of the potential corresponds to Model I by Binney & Tremaine (2008), fitting several of the properties of the Milky Way structure and consisting of two spheroidal components, a dark halo and a bulge, and three

[1] This is referred to as 'churning' when not accompanied by heating of the stellar populations.

disc components: thin, thick, and ISM disc. The mass of the dark halo inside 100 kpc is $M_{\mathrm{h},<100\ \mathrm{kpc}} = 6 \times 10^{11} M_\odot$, and the total mass of the bulge is $M_\mathrm{b} = 5.18 \times 10^9 M_\odot$. The disc densities are exponential both in R and in z. In particular the radial scale length of the thin and thick disc is $h_\mathrm{R} = 2$ kpc, and their scale heights $h_z^\mathrm{thin} = 0.3$ kpc and $h_z^\mathrm{thick} = 1$ kpc. The ISM disc has scale length and height $h_\mathrm{R}^\mathrm{ISM} = 4$ kpc and $h_z^\mathrm{ISM} = 0.08$ kpc respectively, and a hole for $R < 4$ kpc. The total mass of the three disc components is $M_\mathrm{d} = 5.13 \times 10^{10} M_\odot$. In this model the Sun is placed at $(R_0, \phi_0, z_0) = (8\ \mathrm{kpc}, 0, 0)$, i.e., we measure the angles from the line connecting the Sun and the center of the Galaxy.

The bar potential is a 3D version of the pure quadrupole model used by, e.g. Weinberg (1994) and Dehnen (2000). It reads

$$\Phi_\mathrm{b}(R,\phi,z,t) = \alpha \frac{v_0^2}{3} \left(\frac{R_0}{R_\mathrm{b}}\right)^3 U(r) \frac{R^2}{r^2} \cos\gamma_\mathrm{b}, \qquad (1)$$

where $r^2 = R^2 + z^2$ is the spherical radius, R_b is the length of the bar, R_0 is the Galactocentric radius of the Sun, and v_0 is the circular velocity at R_0,

$$\gamma_\mathrm{b}(\phi,t) \equiv 2\left(\phi - \phi_\mathrm{b} - \Omega_\mathrm{b} t\right), \qquad (2)$$

and

$$U(r) \equiv \begin{cases} (r/R_\mathrm{b})^{-3} & \text{for } r \geqslant R_\mathrm{b}, \\ (r/R_\mathrm{b})^3 - 2 & \text{for } r < R_\mathrm{b}. \end{cases} \qquad (3)$$

The amplitude α is the ratio between the bar's and axisymmetric contribution to the radial force, along the bar's long axis at $(R, z) = (R_0, 0)$. We choose for the simulations $\alpha = 0.01$ as in Dehnen (2000), $\Omega_\mathrm{b} = 52.2$ km s^{-1} kpc^{-1} so that $\Omega_\mathrm{b}/\Omega(R_0) = 1.89$ (Antoja et al. 2014), $R_\mathrm{b} = 3.5$ kpc, and ϕ_b such that at the end of the simulations t_e, the bar major axis has a 25° inclination w.r.t. the line connecting the Sun and the center of the Galaxy, i.e., $\phi_\mathrm{b} + \Omega_\mathrm{b} t_\mathrm{e} = 25°$ (Dehnen 2000), where t_e corresponds to the present time. For comparison, in one case (see below) we will present results in the case where $\phi_\mathrm{b} + \Omega_\mathrm{b} t_\mathrm{e} = 45°$. The bar constructed in this way does not modify the Galaxy's total mass and circular velocity curve. The mass of the baryons going into the bar (equal to the integrated positive density part of the bar) is about $4.43 \times 10^9 M_\odot$.

The bar considered here is slightly different from the one of Bovy et al. (2015) in terms of amplitude (our bar is 50 per cent weaker), and vastly different from the one of Wegg et al. (2015) for structure (half-length of the bar 5 kpc) and pattern speed ($\lesssim 45$ km s^{-1}, see also Portail et al. 2015).

It could be that the Galaxy's spiral pattern is composed of multiple modes with different pattern speeds (e.g. Quillen et al. 2011; Sellwood & Carlberg 2014), but observations indicate that the non-axisymmetric part of the old stellar component of the Milky Way disc is dominated by a two-armed spiral pattern outside of the bar region (namely, the Scutum-Centaurus and Perseus arms, Benjamin et al. 2005; Churchwell et al. 2009). Therefore, we consider a spiral perturbation consisting in a two-armed model, in the form originally proposed by Cox & Gómez (2002)

$$\Phi_\mathrm{s}(R,\phi,z,t) = -\frac{A}{R_\mathrm{s} K D} \cos\gamma_\mathrm{s} \left[\mathrm{sech}\left(\frac{Kz}{\beta}\right)\right]^\beta, \qquad (4)$$

where

$$K(R) = \frac{2}{R \sin p}, \qquad (5a)$$

Simulation	bar's α	spiral's A (km^2 s^{-2})	$\phi_\mathrm{b} + \Omega_\mathrm{b} t_\mathrm{e}$
B	0.01	0	25°
B2	0.01	0	45°
S1	0	341.847	-
S2	0	683.694	-
BS1	0.01	341.847	25°
BS2	0.01	683.694	25°
B2S2	0.01	683.694	45°

Table 1. Amplitudes of the perturbation potentials presented in this work.

Resonance	R(kpc)
Bar's corotation	4.08
Bar's OLR	7.22
Spiral arms' corotation	11.49
Spiral arms' ILR	1.89
Spiral arms' inner 4:1 resonance	7.61
Spiral arms' inner 3:1 resonance	6.09

Table 2. Radii of the resonances in all considered models in this work.

$$\beta(R) = K(R) h_\mathrm{s} \left[1 + 0.4 K(R) h_\mathrm{s}\right], \qquad (5b)$$

$$D(R) = \frac{1 + K(R) h_\mathrm{s} + 0.3\left[K(R) h_\mathrm{s}\right]^2}{1 + 0.3 K(R) h_\mathrm{s}}, \qquad (5c)$$

$$\gamma_\mathrm{s}(R,\phi,t) = 2\left[\phi - \phi_\mathrm{s} - \Omega_\mathrm{s} t + \frac{\ln(R/R_\mathrm{s})}{\tan p}\right]. \qquad (5d)$$

Here, p is the pitch angle, A the amplitude of the spiral potential, h_s controls the scale-height of the spiral, and R_s is the reference radius for the angle of the spirals. This potential corresponds to a spiral density distribution

$$\rho_\mathrm{s}(R,\phi,z,t) \approx \rho_0 \frac{K h_\mathrm{s}}{D} \frac{\beta+1}{\beta} \cos\gamma_\mathrm{s} \left[\mathrm{sech}\left(\frac{Kz}{\beta}\right)\right]^{2+\beta}, \qquad (5e)$$

where $\rho_0 = A/(4\pi G R_\mathrm{s} h_\mathrm{s})$. We choose $R_\mathrm{s} = 1$ kpc, $\Omega_\mathrm{s} = 18.9$ km s^{-1} kpc^{-1}, $\phi_\mathrm{s} + \Omega_\mathrm{s} t_\mathrm{e} = -26°$, and $p = -9.9°$ (Siebert et al. 2012; F14; M16). Moreover, we specify two values for A: the first corresponds to a 30 per cent density contrast of the spiral arms w.r.t. the background disc surface density at R_0 ('reference spirals', $A = 341.8$ km^2 s^{-2}), the second to a 60 per cent density contrast ('strong spirals', $A = 683.7$ km^2 s^{-2}). With these values of A, the spiral arms produce a maximum radial force of 0.5 per cent (reference spirals) and 1 per cent (strong spirals) of the force due to the axisymmetric background at $R = R_0$.

We label 'B' the bar-only simulation, 'S1' and 'S2' the simulations with only the reference and strong spirals respectively, and 'BS1' and 'BS2' the simulations with the bar together with the reference and strong spirals respectively. We will also show one case in which the bar is coupled with the strong spirals and $\phi_\mathrm{b} + \Omega_\mathrm{b} t_\mathrm{e} = 45°$ ('B2S2'). The bar-only simulation, with the bar orientation $\phi_\mathrm{b} + \Omega_\mathrm{b} t_\mathrm{e} = 45°$ is labelled 'B2' (Table 1).

2.2 Initial conditions

We generate the disc initial conditions as discrete realizations of the phase-space Shu-Schwarzschild distribution function (Shu 1969; Bienayme & Sechaud 1997; Binney & Tremaine 2008), as explained in F14. In this way we obtain a disc of 5×10^7 particles whose surface density distribution in configuration space is approximately exponential with radius (scale length $h_{\rm R}$), and whose vertical distribution is determined by the restoring force. The radial and vertical velocity dispersion on the disc plane vary approximately as $\sigma_R \approx \sigma_{R,0} \exp\left[-\left(R-R_0\right)/R_\sigma\right]$, $\sigma_z \approx \sigma_{z,0} \exp\left[-\left(R-R_0\right)/R_\sigma\right]$, where $(\sigma_{R,0}, \sigma_{z,0}) = (35, 15)$ km s^{-1}, and $R_\sigma = 5h_{\rm R}$ (Bienayme & Sechaud 1997, F14). The test particles distribution obtained with these parameters resemble the thin disc of Section 2.1, which is the only stellar disc modeled with test particles.

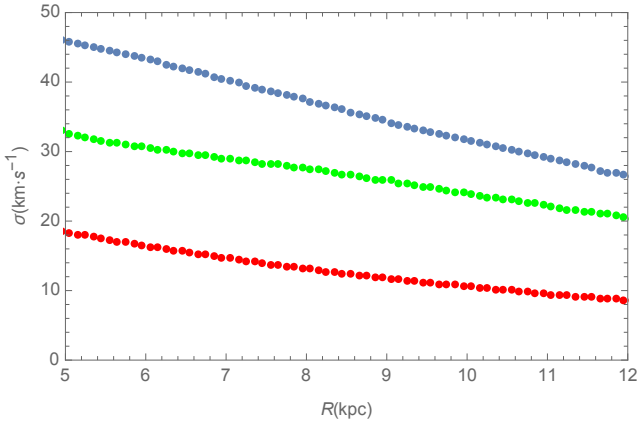

Figure 1. Velocity dispersion of the disc test particles with $|z| < 0.5$ kpc at $t = 0$, as a function of R. Blue dots: radial velocity dispersion σ_R. Green dots: tangential velocity dispersion σ_ϕ. Red dots: vertical velocity dispersion σ_z.

2.3 Time scales

We integrate forward our initial conditions for a total time $T = 9$ Gyr, from $t_{\rm i} = -3$ Gyr to $t_{\rm e} = 6$ Gyr.

For $t < 0$ we integrate the initial conditions in the axisymmetric part of the potential only. We do this so that the initial conditions become mixed with the background potential[2]. After the initial 3 Gyr, we obtain stable distribution functions in the Model 1 of Binney & Tremaine (2008) potential, with velocity dispersions at $(R, z) = (R_0, 0)$: $(\sigma_R, \sigma_\phi, \sigma_z) \approx (37, 27, 13)$ km s^{-1} (see Fig. 1). The vertical restoring force determines the z density profile. At $R = R_0$ this is nicely fitted by a sech^2 profile with scale height $h_z \approx 0.3$ kpc. In Fig. 2 we compare the density of test particles after the mixing time with the density of the thin disc in the background potential. The radial profiles (top panel) are in excellent agreement over a large range of radii, and diverge only in the central parts because of the tapering of the initial conditions at $R < 4$ kpc (see F14). The vertical profile (bottom panel) differs only slightly from the one of the thin disc of the background potential which is purely exponential, because of the form of the distribution function used to generate the test particles initial conditions.

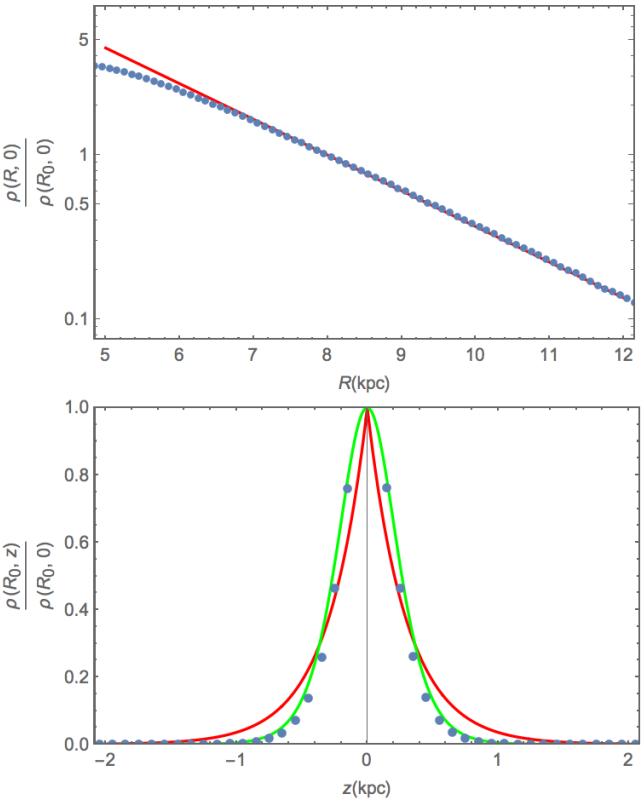

Figure 2. Profiles for the disc test particles density at $t = 0$ (blue dots), and the volume density $\rho_{\rm thin}$ of the thin disc (red line) of Model I by Binney & Tremaine (2008), used here as a background potential. Top panel: radial density profile of particles with $|z| < 0.3$ kpc compared with $\rho_{\rm thin}(R, 0)$. Bottom panel: vertical density profile of particles with $|R - R_0| < 0.3$ kpc (blue dots) compared with $\rho_{\rm thin}(R_0, z)$ (red line); the green line is the function $f(z) = \text{sech}^2(z/(0.3\text{ kpc}))$.

The bar and the spiral arms forces are present in the simulations only for $t > 0$. These are introduced in the simulations by letting their respective amplitudes α and A grow by a factor (Dehnen 2000)

$$\eta(t) = \left(\frac{3}{16}\xi^5 - \frac{5}{8}\xi^3 + \frac{15}{16}\xi + \frac{1}{2}\right), \quad \xi \equiv 2\frac{t}{3\text{ Gyr}} - 1, \quad (6)$$

until, at $t = 3$ Gyr they reach their final amplitude which is kept constant until the end of the simulation at $t = t_{\rm e} \equiv 6$ Gyr.

[2] Since the Shu-Schwarzschild distribution function is built on approximated integrals of motion, because of Jeans' Theorem, it will evolve. The faster, the worse the approximation of the integrals.

3 PECULIAR L.O.S. VELOCITY POWER SPECTRUM

In a recent paper, Bovy et al. (2015) proposed a method to characterise the peculiar velocity field of the disc stars using a pencil beam survey, where the spectroscopic information (i.e. the line of sight $v_{\rm los}$ velocity) and the photometric distance of the stars are estimated (as it happens for the APOGEE survey, Majewski et al. 2015). This method analyses the power spectrum of the peculiar line of sight (l.o.s.) velocity (see below for a definition), and the observed power spectrum was tested by Bovy et al. (2015) on some simple simulations, including a bar or spiral arms. These tests showed a striking difference in the spectra induced by the bar and spiral arms models considered.

Grand et al. (2015a) computed the power spectrum of the kinematics of more sophisticated N-body models of disc galaxies and found that this is sensitive to parameters such as the number of spiral arms, spiral arm pitch angle, and position of the Sun with respect to the spiral arm. In particular, they consider the power spectrum of the peculiar line of sight velocity projected on the Galactic plane, defined as

$$\begin{aligned}\tilde{v}_{\rm los}\mathbf{e}_{\rm los} \quad \equiv \quad & \langle v_R\rangle \cos b \cos(\pi-\phi-l)\mathbf{e}_R + \\ & (\langle v_\phi\rangle - \langle v_{\phi,0}\rangle)\cos b \sin(\pi-\phi-l)\mathbf{e}_\phi, \end{aligned} \tag{7}$$

where

$$\langle v_{\phi,0}\rangle \equiv \frac{1}{2\pi}\int_0^{2\pi}\langle v_\phi\rangle \, {\rm d}\phi, \tag{8}$$

$\mathbf{e}_R$, $\mathbf{e}_\phi$, and $\mathbf{e}_{\rm los}$ are the versors in the radial, tangential and l.o.s. direction, l and b are the Galactic longitude and latitude, and the averages $\langle\cdot\rangle$ are computed at some position (R,ϕ) of the Galactic plane. In this work l and b are computed assuming the Sun at $(R,\phi,z) = (8\ {\rm kpc}, 0, 0)$. The quantity $\tilde{v}_{\rm los}$ represents the difference between the mean l.o.s. velocity and the mean l.o.s. velocity of the axisymmetric background. To compute the power spectrum, $\tilde{v}_{\rm los}$ is evaluated on a $N\times N$ grid in $x\equiv R\cos\phi$ and $y\equiv R\sin\phi$, so that the power $P(k_x,k_y)$ is

$$P\left(k_x,k_y\right) = (4\pi)^2\left|F\left(k_x,k_y\right)\right|^2, \tag{9}$$

where $F\left(k_x,k_y\right)$ is the discrete Fourier transform of $\tilde{v}_{\rm los}(x,y)$ on the $N\times N$ grid (k_x and k_y are in units of ${\rm kpc}^{-1}$, and P in units of ${\rm km^2 s^{-2}}$). In particular, $P\left(k_x,k_y\right)$ is estimated at the wavenumbers $(k_x,k_y) = (k_{\rm max}l/N, k_{\rm max}m/N)$, with $l = 1,...,N$, $m = 1,...,N$, and $k_{\rm max}$ is the Nyquist wavenumber. The one-dimensional power spectrum $P(k)$ is computed by averaging $P\left(k_x,k_y\right)$ along rings in the k_x-k_y plane (for the details see Bovy et al. 2015; Grand et al. 2015a).

Here, as in Bovy et al. (2015) and Grand et al. (2015a) we estimate $P(k)$ in a portion of the disc resembling the one spanned from the APOGEE survey, i.e., $x\in[5.5\ {\rm kpc}, 12.5\ {\rm kpc}]$, $y\in[-3.5\ {\rm kpc}, 4.5\ {\rm kpc}]$, and $|z| < 0.25$ kpc. The $x-y$ grid has bin size 0.8 kpc. In Fig. 3 (top) we show this power spectrum for the several models. The first thing we note is that while the spiral models (S1 and S2) bear some resemblance with Bovy et al. (2015) spiral models (even though they do not peak as strongly at $k\lesssim 1\ {\rm kpc}^{-1}$), their bar model has a very strong peak at $k\sim 0.5\ {\rm kpc}^{-1}$, that is not present in the spectra of this

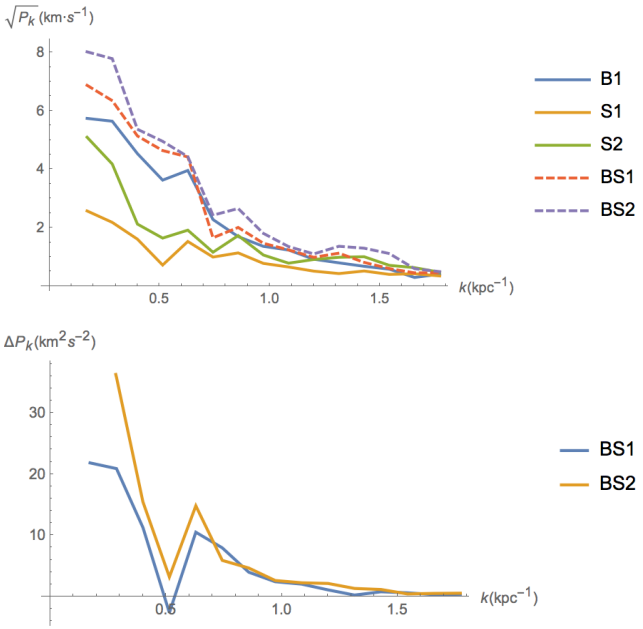

Figure 3. Top: power spectrum $\sqrt{P_k}$ for all the simulations, computed in a volume similar to the one spanned by APOGEE. Bottom: ΔP_k for the BS1 and BS2 cases respectively.

work[3]. We associate these differences both to the fact that their fiducial bar model grows faster (their slowly grown model is more similar to ours), and that their perturbation is 50 per cent times stronger than ours (and of Dehnen 2000). In fact, all our spectra resemble more their $m = 2$ elliptical perturbations, with most of the power on large scales. Linear theory predicts that, at least away from the resonances (Table 2), $\tilde{v}_{\rm los}$ scales linearly with the strength of the perturbation, and so do $\sqrt{P_k}\propto|\tilde{v}_{\rm los}|$. Therefore, the strength of the perturbation mostly influences the amplitude of the power spectrum. Another significant factor in shaping the power spectrum, and in particular the relative height of the peaks, is the volume of configuration space on which the power spectrum is computed. This might explain differences with the APOGEE data points. Bovy et al. (2015) compute the power spectrum of their synthetic models with the bar in the same volume of configuration space as the one we use, but the time scales of their simulations are different. This can cause significant non-stationary features in the velocity field (see Section 4.1) that disappear as the disc gets more phase-mixed, and which can influence the power spectrum. Notice that, while the circular velocity curve and position of the resonances in the synthetic models of Bovy et al. (2015) are similar to those in the simulations of the present work, other differences could contribute to create a different power spectrum: the 2D nature of the simulations of Bovy et al. (2015) versus the 3D nature of our simulations, a slightly kinematically colder disc ($\sigma_R(R_0) = 31.4$ km s^{-1} in their case), and a longer scale length ($h_{\rm R} = 3$ kpc). Using the linear theory of M16 we found that a $h_{\rm R} = 3$ kpc scale length decreases the power on the largest scales, while the

[3] The same peak is also present in the barred model presented in Grand et al. (2015a).

differences with the $\sigma_R(R_0) = 31.4$ km s^{-1} case are not significant. However, these effects are small, if compared to the differences due to a different volume for the computation of the power spectrum, notably when comparing to APOGEE data and the intrinsic selection function of the survey.

The models with the combination of bar and spiral arms present a larger power of the peculiar l.o.s. velocity at all scales (but mostly on large scales), with the model BS2 having larger power than BS1. However, apart from the larger overall power of these models, their spectra do not present striking qualitative differences with respect to the other models (e.g. peaks of power at some particular scale not present in the other cases). Therefore, we can ask ourselves whether the power in the combined bar and spiral arms case is simply the power obtained by linearly summing the single $\tilde{v}_{\rm los}$ fields induced independently by the bar and spiral arms. Since the power goes as the square of the peculiar velocity, we have

$$P_{k,\rm BS} \leqslant P_{k,\rm B} + P_{k,\rm S} + 2\sqrt{P_{k,\rm B}P_{k,\rm S}}, \tag{10}$$

where $P_{k,\rm B}$, $P_{k,\rm S}$, and $P_{k,\rm BS}$ are the powers in the bar, spiral arms, and coupled case respectively. In Fig. 3 (bottom) we plot the quantity

$$\Delta P_k \equiv P_{k,\rm B} + P_{k,\rm S} + 2\sqrt{P_{k,\rm B}P_{k,\rm S}} - P_{k,\rm BS}. \tag{11}$$

If $\Delta P_k \geqslant 0$ the condition equation (10) is respected. This condition is *necessary but not sufficient* to say that the peculiar velocity is simply the sum of the peculiar velocity induced by the bar and the spiral arms everywhere in the disc. Fig. 3 (bottom) shows that this condition is respected almost everywhere in our simulations. We will hereafter turn to the detailed 3D velocity field to see whether the superposition really is linear. Nevertheless, the power spectrum in the fashion of Bovy et al. (2015) clearly indicates that the APOGEE large-scale velocity fluctuations are probably predominantly driven by the bar unless the spiral arm with a large amplitude is a transient and corotating as suggested by Grand et al. (2015a), and that the addition of spirals does not change much, except for the addition of power on the largest scales. This means that adding to a bar-only model quasi-static spirals with density contrast as large as 60 per cent also provides an acceptable fit. The amplitude of spirals certainly does not have to be negligible for the power spectrum to match APOGEE observations. Also, this does not prevent the spirals from having non-negligible influences at specific radii linked to resonance overlaps (notably in terms of churning), and on mean vertical motions, as we investigate hereafter through a detailed analysis of the 3D velocity field.

4 ANALYSIS OF THE 3D VELOCITY FIELD

4.1 Bar simulation

In Fig. 4 we show the result of the simulation B. The 3 panels represent the average of the velocity components of the particles at $t = t_{\rm e}$ on the $(x, y) \equiv (R\cos\phi, R\sin\phi)$ plane, inside square bins of size 250 pc. The left panel represents $\langle v_R\rangle$, the central panel $\langle v_\phi\rangle - \langle v_{\phi,0}\rangle$, and the right the quantity $\Delta\langle v_z\rangle$, i.e., the difference between $\langle v_z\rangle$ for $z > 0$ and for $z < 0$ (see M15).

The average of the 3 velocity components has the form, at every R, of a $m = 2$ Fourier mode. These results are, at least far from the resonances, in agreement with the findings of Kuijken & Tremaine (1991) that studied the response of the horizontal kinematics (v_R and v_ϕ) to perturbations in 2D stellar discs, and with M15 that related the mean v_z to the average v_R and v_ϕ in 3D, and noticed for the first time that the bar induces non-zero mean vertical motions in the whole Galaxy (even though of very small amplitude). At the resonances (dashed circles) the effects of the perturbation are always special. For v_R we notice that the streaming motions induced by the bar are particularly strong near the resonances, and that the phase of the Fourier mode changes by 90° passing from inside to outside the OLR . These effects can be related to particular orbital configuration induced by the bar nearby the resonances (M15, Binney & Tremaine 2008). The strongest effects on the v_ϕ component are just outside the corotation. Notice how, just outside the OLR, the behaviour of v_ϕ is not described by the linear approximation, that would predict the maxima (minima) of $\langle v_\phi\rangle - \langle v_{\phi,0}\rangle$ aligned with the long (short) axis of the bar. This prediction is eventually confirmed only at $R \sim 9$ kpc. This behavior was also observed by Mühlbauer & Dehnen (2003) in the case of their hotter models. Finally, we plot the difference $\Delta\langle v_z\rangle$ between the mean motion for particles with $z > 0$ and $z < 0$, as in M15, a quantity which is positive (negative), i.e. corresponds to a rarefaction (compression) for particles that move away from (towards) the Galactic plane. In the case of B this breathing mode is always quite moderate, and changes phase (of an angle of 90°) at the OLR, as predicted in M15.

4.2 Spiral arms simulations

The results of the S1 and S2 simulations show an agreement with the models of M16 and a qualitative agreement with the simulations of F14 and Debattista (2014). Figs. 5-6 illustrate it, with the same meaning of the left, central, and right panel as in Fig. 4. In these plots we only show the locus of the spiral arms (thick red curves) since there are no major resonances in the plotted regions. As already observed in F14 and M16, the average velocity contours have the shape of two-armed Fourier modes resembling to spiral arms. In particular, the locus of the spiral arms correspond with the maximum amplitude of the v_R streaming motion, directed towards the center of the Galaxy in the arms region, and outwards in the interarm regions (within corotation). The breathing mode is $\Delta\langle v_z\rangle = 0$ on the arms, and $\Delta\langle v_z\rangle < 0$ ($\Delta\langle v_z\rangle > 0$) in the trailing (leading) edge of the arms (within corotation). Contrary to the case of the bar, there is thus a phase shift between the maxima of vertical and radial bulk motions, a phase shift which is linked to the oscillatory nature of the radial part of the spiral potential, contrary to the case of the bar (see M15). The v_ϕ velocity (not treated by F14) exhibits more complicated patterns, however the general effect is a weak tendency for the stars to move faster outside of spiral arms and slower inside.

The differences with F14 are quantitative. The kinematic responses are much larger in their case. This is not surprising, considering that the maximum radial force of the F14 spirals at R_0 and relative to the axisymmetric background was 0.23, while it is 0.05 and 0.1 for S1 and S2 respectively in the present case. Moreover, the vertical force

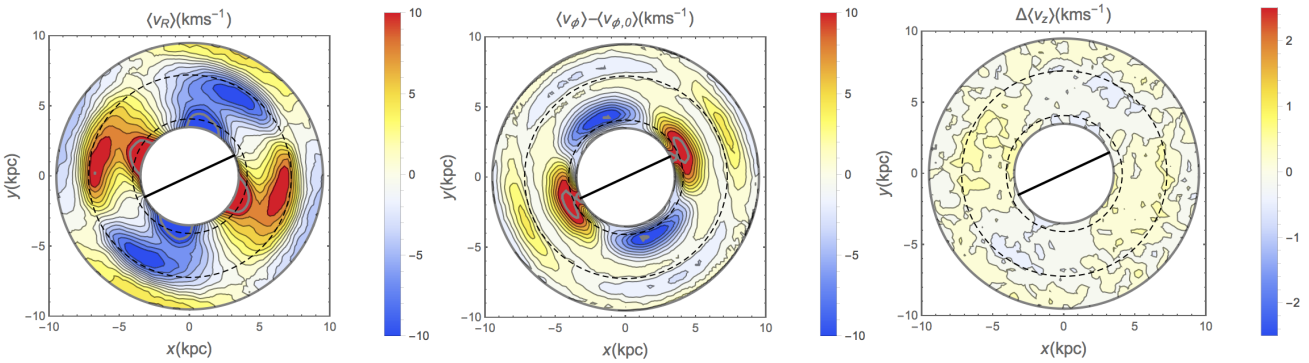

Figure 4. Average velocities at $t = t_e$ for the simulation B on x vs. y plane. Left panel: $\langle v_R \rangle$. Center: $\langle v_\phi \rangle$. Right: $\Delta\langle v_z \rangle$. The averages are computed inside square bins of size 0.25 kpc. A Gaussian filter on a scale 0.5 kpc is applied to the maps. The thick line at the center of the panels represents the long axis of the bar. The dashed circles represent the position of the corotation and OLR . The Galaxy rotates anti-clockwise.

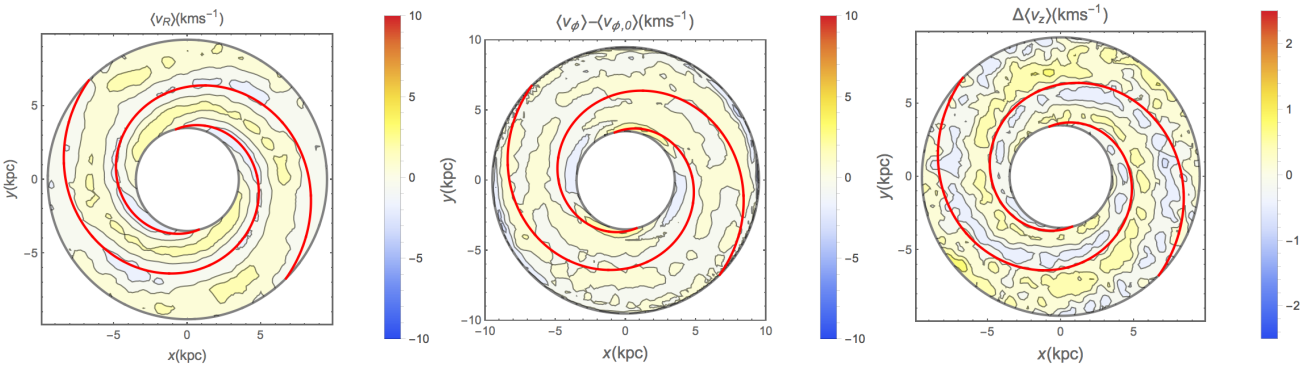

Figure 5. Average velocities at $t = t_e$ for the simulation S1 on x vs. y plane. Left panel: $\langle v_R \rangle$. Center: $\langle v_\phi \rangle$. Right: $\Delta\langle v_z \rangle$. The averages are computed inside square bins of size 0.25 kpc. A Gaussian filter on a scale 0.5 kpc is applied to the maps. The thick red line represents the locus of the spiral arms.

exerted by the F14 spiral arms is much stronger than in the present cases. Note that the Cox & Gómez (2002) model that we use is more realistic, as it is the one related by the Poisson equation to spiral arms that have a realistic density $\approx \mathrm{sech}^2$ density fall-off in z.

4.3 Coupled bar-spiral simulations

We now focus on the main topic of this paper, namely the effects of bar-spiral couplings on stellar kinematics. Fig. 7 and Fig. 8 represent the kinematical response of our simulations in the case where both the bar and the spiral arms are present (BS1 and BS2 respectively). The first glance at these figures shows how the bar seems to dominate the horizontal motions (v_R and v_ϕ), in line with the analysis of the power spectrum, while the vertical motions have the shape of spiral arms. However, concerning vertical motions, comparing Fig. 7 with Fig. 5, and Fig. 8 with Fig. 6 we see that the effect of the bar in $\Delta\langle v_z \rangle$ is to enhance the amplitude of the breathing mode and to shift the position of the 'vertical kinematic spiral arms' w.r.t. the locus of the spiral arms. In particular, while in Figs. 5-6 the locus of the spiral arms coincides with the passage from $\Delta\langle v_z \rangle > 0$ to $\Delta\langle v_z \rangle < 0$, in Figs. 7-8 the locus of the arms corresponds with minima of $\Delta\langle v_z \rangle$ (i.e. regions where the particles move on average towards the Galactic plane).

It is at this point important to quantify the non-linear effects of the coupling of the bar and spirals on mean motions by comparing the kinematics of our coupled simulations with the linear combination of the single effect of these two perturbers. To study this, we use the quantities

$$\delta q \equiv q^{\mathrm{BS}} - \left(q^{\mathrm{B}} + q^{\mathrm{S}} \right), \tag{12}$$

where the superscripts B, S, and BS refer to estimating the quantities in the bar, spirals (reference or strong), and bar and spirals simulations respectively, whilst the quantity q will be, respectively, $\langle v_R \rangle$, $\langle \tilde{v_\phi} \rangle \equiv \langle v_\phi \rangle - \langle v_{\phi,0} \rangle$, and $\Delta\langle v_z \rangle$. The δ quantities represent the kinematic difference between the models where the coupling between the bar and the spiral arms is present and the linear combination of the effects of the bar and spiral arms alone. Fig. 9 shows, from left to right, the quantities $\delta\langle v_R \rangle$, $\delta\langle \tilde{v_\phi} \rangle$, $\delta\Delta\langle v_z \rangle$ for the BS2 simulations. The $\delta\langle v_R \rangle$ panel reveals that significant non-linear effects due to the coupling are restricted only to few regions of the Galactic plane, especially at the tip of the bar, and at the OLR, where resonance overlaps with low order resonances of the spirals are taking place.

The $\Delta\langle v_z \rangle$ case is different. In this case, the regions where $\delta\Delta\langle v_z \rangle$ has a similar amplitude to $\Delta\langle v_z \rangle$ in the spiral arms case extend in a large area of the Galactic plane, and have a form that resembles spiral arms. In the arms regions $\delta\Delta\langle v_z \rangle$ is negative (i.e. there is a surplus 'compression' of

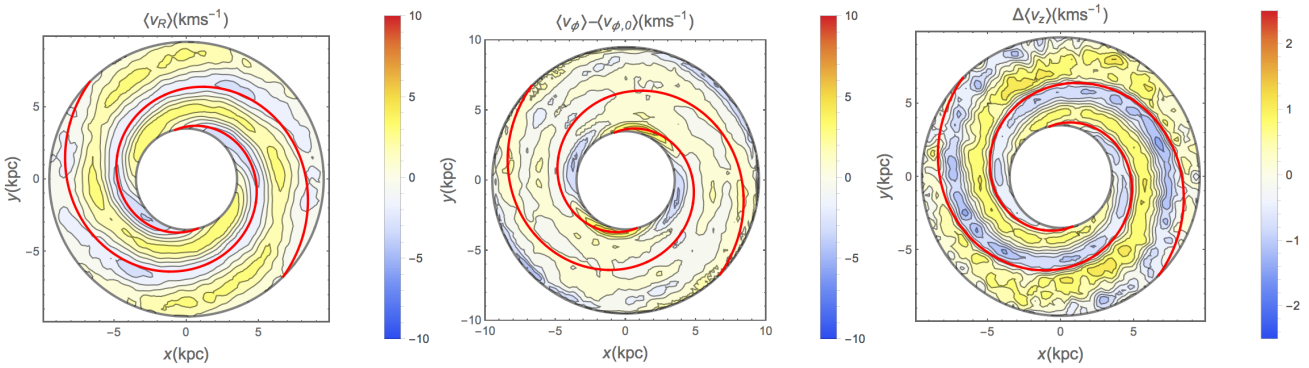

Figure 6. As in Fig. 5, but for S2.

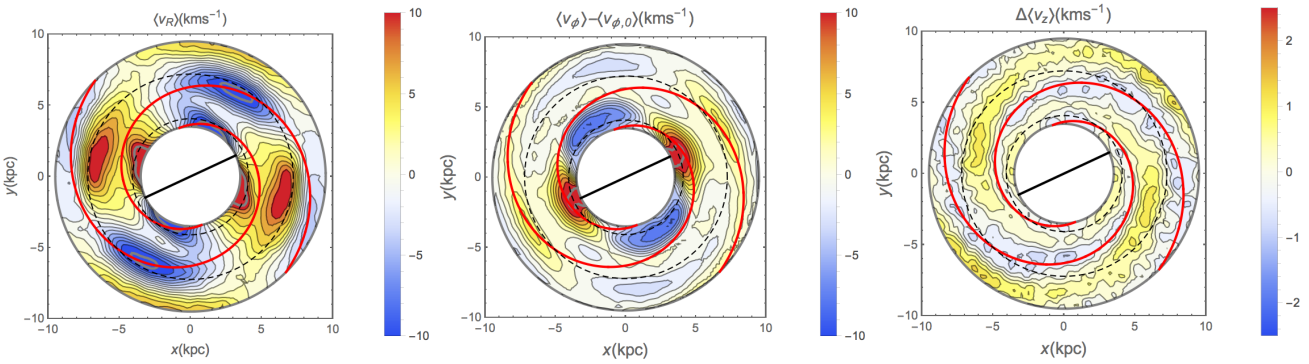

Figure 7. As in Fig. 4, but for BS1.

the breathing modes), while it is positive in the interarm regions (i.e. there is a surplus 'rarefaction' of the breathing mode). Notice that this implies, in some regions, a change in the sign of $\Delta\langle v_z\rangle$, i.e. the passage from a compression to a rarefaction breathing mode. This happens for example just outside the loci of the spiral arms.

This particular configuration of $\delta\Delta\langle v_z\rangle$ is not specific to the particular bar and spiral arms orientation: in Fig. 10 we have the same plot for the simulation B2S2, where the bar long axis is oriented at $\phi = 45°$ from the Sun, and we still have $\delta\Delta\langle v_z\rangle < 0$ on the arms and $\delta\Delta\langle v_z\rangle > 0$ in the interarm regions. This behaviour of $\delta\Delta\langle v_z\rangle$ is a major new result, which could help explain from non-axisymmetries alone the amplitude of the observed breathing mode in the extended Solar neighbourhood, which will be quantified more precisely with forthcoming Gaia data. We however note that the simulations presented here never reach the amplitude reported by the current observations (Widrow et al. 2012; Williams et al. 2013; Carlin et al. 2013) which, at least far from the Galactic plane, can even rise to $|\langle v_z\rangle| \sim 15$ km s^{-1}. However, the bulk of particles that we study in our simulations is closer to the Galactic plane ($|z| < 0.3$ kpc), where the observed gradient is of the order of $\sim 10^{-2}$ km s^{-1} pc^{-1}, thereby reaching $|v_z| \sim 3$ km s^{-1} at $z = 0.3$ kpc. Such amplitudes are almost twice as high as our BS2 values and could probably be reproduced using other models of spiral arms with a stronger vertical force (for example, when the scale height h_s is smaller). In any case, the non-linear enhancement of the breathing modes in the coupled case is a non-negligible effect to take into account in future modelling, and will have

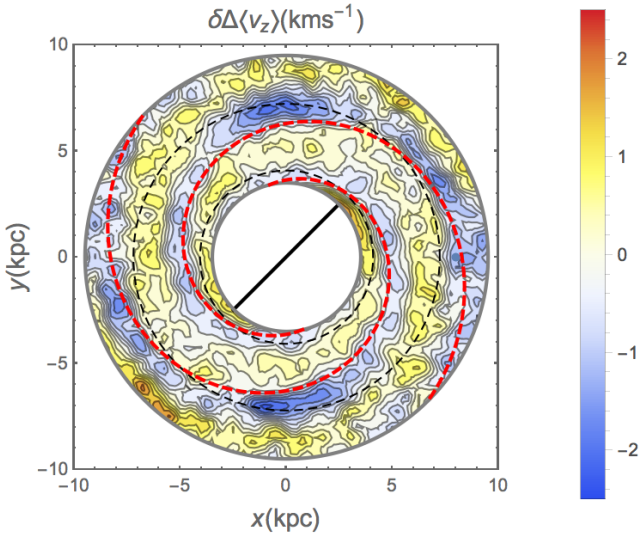

Figure 10. As in Fig. 9, right panel, but for the simulation B2S2 compared to B2+S2.

to be understood theoretically by coupling two perturbers in analytical models of the type developed in M16.

5 RADIAL MIGRATION

Of particular importance is the effect of non-axisymmetries of the Galactic disc on the chemical enrichment of the stars

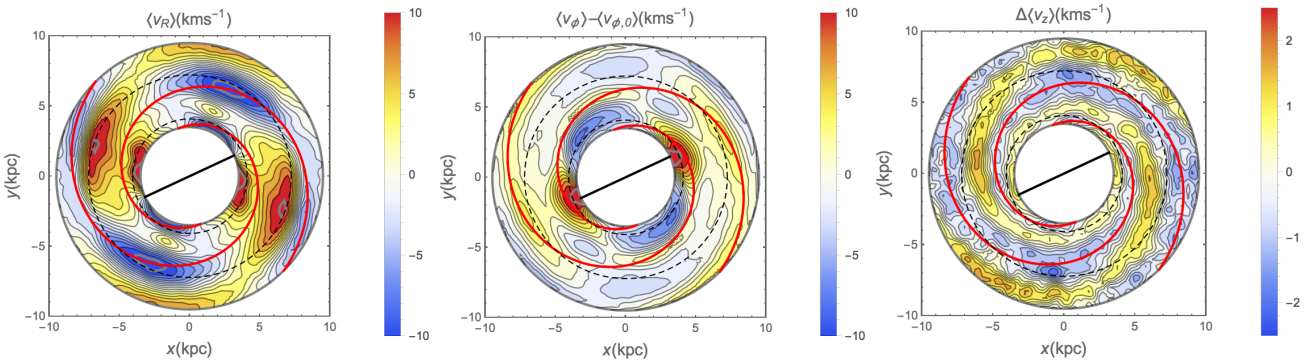

Figure 8. As in Fig. 4, but for BS2.

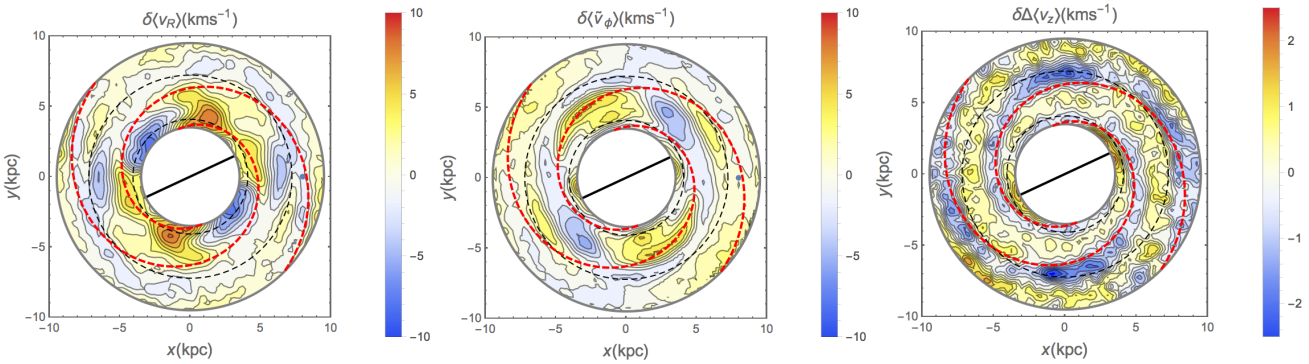

Figure 9. Comparing the kinematic effects of simulations B+S2 with simulation BS2 at $t = 6$ Gyr. Left: $\delta\langle v_R\rangle$ in the x vs. y plane. Center: $\delta\langle v_\phi\rangle$ in the x vs. y plane. Right: $\delta\Delta\langle v_z\rangle$ in the x vs. y plane. Bin sizes 0.25 kpc. See Eq. 12 for the definition of the plotted quantities.

and the chemical evolution of the Galactic disc. The distribution of chemical abundances and ages in the Solar neighbourhood seems to be incompatible with a simple model where the stars are born from progressively metal enriched cold gas at a given radius, and which does not change except for the oscillations due to the eccentricity of their orbits (e.g. Sellwood & Binney 2002). The exact amount of so-called 'radial migration" needed in chemical evolution models to explain observations is nevertheless subject to much debate (Minchev et al. 2013; Kubryk et al. 2015; Haywood et al. 2016).

This mechanism is linked to the non-axisymmetric structures of the Milky Way moving the guiding centre of the stars' orbits around the disc via resonant trapping, without changing their eccentricities. This is also referred to as 'churning', to not be confused with 'blurring' corresponding to the increase in velocity dispersions which can also make stars span wider radii, but without changing their guiding radius. The radial migration mechanism originally proposed by Sellwood & Binney (2002) involves transient spirals, which trap stars on horseshoe orbits close to their corotation before fading away, and thus prevents stars from returning to their initial guiding radius. This effect has been shown to be significantly increased in the presence of multiple spiral patterns of different angular speed, or in the case of the coupling of the bar and spiral arms (Minchev & Famaey 2010). This increase has been attributed to resonance overlaps (Chirikov 1979), i.e. that an orbit is trapped first by one resonance with one pattern, and then by another one with the other pattern, with the times of transition between resonantly trapped families varying erratically. This chaotic behaviour can enhance churning indeed, but can at the same time cause some blurring of the orbits.

In this Section we reanalyse the pure effect of resonance overlap on the amount of radial migration in our simulations for which amplitudes are *not* varying once the perturbations have settled, in the spirit of Minchev & Famaey (2010), but this time in 3D and with low-order resonance overlaps. In Fig. 11 we show the change of guiding center radii induced by the bar and spiral arms, for a selection of particles with low eccentricity ($e < 0.01$) at the end of our simulations. In this way we aim to separate the particles that actually migrated ('churning') from the 'blurring' of the disc (see, Sellwood & Binney 2002), which might affect all particles in the disc (orange contours in Fig. 11). The initial guiding center radius $R_{\rm g,0}$ is computed at the moment when spiral arms and the bar are completely grown ($t = 3$ Gyr), while the final one is at the end of the simulation ($t = 6$ Gyr). The guiding centers $R_{\rm g}$ are found solving the equation $R_{\rm g}^2\Omega(R_{\rm g}) = L_z$ for each particle with angular momentum L_z. The (epicyclic) eccentricity e is estimated (e.g. Dehnen 1999) using

$$e = \sqrt{\frac{v_R^2 + \kappa^2(R_{\rm g})(R - R_{\rm g})^2}{\kappa^2(R_{\rm g})R_{\rm g}^2}}. \qquad (13)$$

The percentage of particles on almost circular orbits (i.e. with $e < 0.01$) is ~ 0.2 per cent in our simulations.

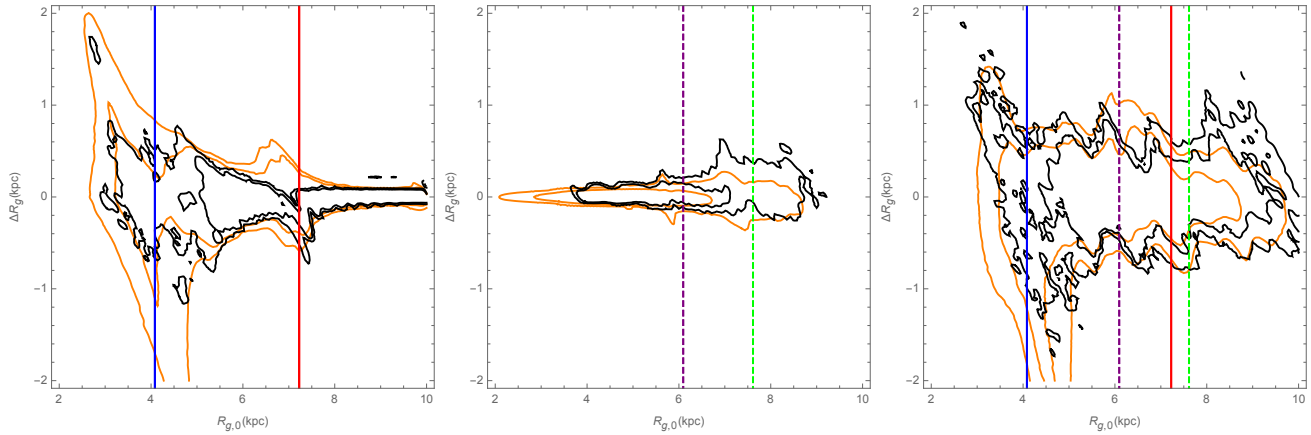

Figure 11. Distribution of the particles in our simulations in the space $R_{\rm g,0}$ vs. $\Delta R_{\rm g}$, where $R_{\rm g,0}$ is the guiding radius estimated $t = 3$ Gyr, and $\Delta R_{\rm g} = R_{\rm g} - R_{\rm g,0}$ with $R_{\rm g}$ estimated at $t = 6$ Gyr. The black contours represent particles that have eccentricity $e < 0.01$ at $t = 6$ Gyr, while the orange contours all the particles. The contours include respectively 68 per cent and 90 per cent of the particles. Left panel: B simulation. Central panel: S2 simulation. Right panel: BS2 simulation. The vertical lines represent the position of the resonances: the solid ones with the bar and the dashed ones with the spiral arms. In particular, the blue and red lines are the bar's corotation and OLR s respectively, and the violet and green lines the $\kappa : (\Omega - \Omega_{\rm s}) = 3 : 1$, and $\kappa : (\Omega - \Omega_{\rm s}) = 4 : 1$.

Fig. 11 shows that, while in the case of the single perturbations radial migration is very limited as expected for non-varying amplitudes, the coupled effects of bar and spiral arms, is not simply the sum of their single effects. Rather, because of the coupling, the stars migrate in the whole range of radii that we consider, and the amplitude of the migration is strongly enhanced, with 32 per cent of low-eccentricity orbits being transported without heating on scales of at least ~ 0.8 kpc, and 10 per cent more than 1 kpc in the outer disc.

This result is in qualitative agreement with the 2D study of Minchev & Famaey (2010), who showed that churning can be driven even by static density waves provided resonance overlaps of multiple patterns are present. With the parameters adopted here, it appears clearly that this mechanism is indeed real, albeit more limited in amplitude than what can be expected from scattering at corotation of transient spirals (Sellwood & Binney 2002), and much more limited than in the models of Minchev & Famaey (2010). The differences in the amplitude of the migration between most of these previous simulations and the present ones should be ascribed to the different combination of parameters and spiral arm models. Indeed, in Minchev & Famaey (2010) the most efficient radial migration was reached when the corotation of one pattern was overlapping with the first-order Lindblad resonance of the other one (for instance if the corotation of the spiral coincides with the OLR of the bar, or if the spiral is four-armed and its 4:1 inner Lindblad resonance coincide with the bar's OLR). In our case, the strongest overlap is between the OLR of the bar and the 3:1 and 4:1 inner resonances of the two-armed spiral, hence lower-order resonances than the corotation or inner Lindblad resonance. The effect of these two low-order resonances of the spiral on churning, as well as the effect of the bar's OLR, is nevertheless clearly visible as distinct peaks in the rightmost panel of Fig. 11. Together with this, the spiral arms used in the models by Minchev & Famaey (2010) (the 'TWA spiral arms') are stronger than the spiral arms used in our simulations in the regions with $R < R_0$. For example, taking a maximum radial force of the spirals as 1 per cent of the force due to the axisymmetric background at $R = R_0$ for both models, the force due to the TWA spiral arms is ~ 1.5 (~ 2) times larger than that of our spiral arms at $R = 6$ kpc ($R = 5$ kpc). Moreover, Minchev & Famaey (2010) consider a range of amplitudes going from 0.5 per cent to 3 per cent of the background force. Finally, the fact that our simulations are 3D reduces the impact of the perturbing force for stars with large oscillations outside of the Galactic plane, where the bar and spiral arms radial and tangential forces are weaker (however, this is not the case of the particles with $e < 0.01$, which spend most of their orbits close the Galactic plane). We thus note that, if the spiral pattern of the Milky Way is a quasi-static density wave with realistic parameters as chosen here, disc metallicity gradients would actually be unaffected by churning; it would not be possible to explain the age-metallicity relation at the solar vicinity, since differences in metallicity of (at least) 0.5 dex, as those observed at all ages among thin disc stars, would require migration to occur on several-kpc scale ($\sim 5-6$ kpc) for a metallicity gradient of 0.1 dex/kpc, that is at least a factor 5 higher than the scale of migration found in our models. On the other hand, some simulations (e.g. Sellwood & Carlberg 2014) tend to show that quasi-static modes do not survive more than 10 rotation periods at corotation (~ 1 Gyr), thereby also causing migration by scattering at corotation (Sellwood & Binney 2002). Other models with co-rotating spirals display even more drastic migration through this corotation mechanism (Kawata et al. 2014). The exact nature of spirals is thus of fundamental importance for theoretically quantifying radial migration, as our models clearly show that, even though migration is indeed happening also when spirals are kept static, the scale of migration is actually extremely limited when adopting realistic parameters for the Milky Way spiral arms.

In our simulations we also recognize a fraction of orbits that cross the bar's OLR: in the simulation with only the bar we count ~ 2 per cent of them, with or without the cut in eccentricity. If we restrict to the least eccentric orbits

(as defined above) which have $|R_{\rm g,0} - R_{\rm OLR}| < 1$ kpc at $t = 3$ Gyr (the time when both bar and spiral arms are fully grown and kept constant in amplitude afterwards), this fraction increases to ~ 10 per cent. Note that there is both absorption and emission in the coupled case. However, at the quantitative level, our model is not really in contradiction with the findings of Halle et al. (2015) who suggested that the OLR limits the exchange of angular momentum between the inner and outer disc. In fact, the mean amplitude of the excursions in guiding radius of the particles that cross the OLR in our bar simulation is moderate (~ 0.3 kpc for all the particles, and ~ 0.5 kpc for the least eccentric orbits), if compared to the rms epicyclic amplitude (for all stars) at $R = R_{\rm OLR}$ (~ 1.2 kpc). Taking into account that the OLR region has non-null thickness (e.g. Ceverino & Klypin 2007), makes the interpretation of these results even more complicated.

6 PREDICTIONS FOR DEEP SPECTROSCOPIC SURVEYS

Ongoing and forthcoming spectroscopic surveys of the Galaxy will be extremely useful to disentangle the effects of the bar and spirals in the Galaxy. As we have seen here, the in-plane peculiar velocity power spectrum is dominated by the bar, and hence makes it difficult to constrain the effect of spirals. In this respect, constraining the local vertical breathing mode might yield a lot of information on the spirals, but this could be difficult to disentangle from other external effects in the outer disc, such as bombarding of the disc by small dark matter sub-halos (Grand et al. 2015b; Gómez et al. 2016). In the inner disc, obtaining exquisite constraints on the breathing mode in 3D could on the other hand be difficult due to the absence of good enough astrometric data, even with the advent of Gaia (for this, we will need to wait for Theia, Jasmine, and WFIRST, Spergel et al. 2009; Gouda et al. 2006; Content et al. 2013). Nevertheless, in Fig. 12 we show how a large spectroscopic survey (e.g. APOGEE and WEAVE, Majewski et al. 2015; Dalton et al. 2012) *alone* (i.e. without supplementary information on proper motions) can be used to probe the effect of the breathing mode and disentangle between different models of the non-axisymmetries in the Milky Way disc (for a similar analysis, in the Gaia case, see Antoja et al. 2016). We consider the differential line of sight velocity $\tilde{v}_{\rm los}$, this time defined as $\tilde{v}_{\rm los} = v_{\rm los} - v_{\rm los,0}$, where

$$v_{\rm los} = \frac{(x-x_0)v_x + (y-y_0)v_y + (z-z_0)v_z}{d}, \qquad (14)$$

$(x_0, y_0, z_0) = (8, 0, 0)$ are the coordinates of the Sun, and $v_{\rm los,0}$ is the projected $\langle v_{\phi,0} \rangle$ on the line-of-sight. We plot $\tilde{v}_{\rm los}$ as a function of the distance from the Sun d, and the Galactic longitude l, for the simulations B, S2, and BS2 (top left, top right, and bottom left panel respectively in Fig. 12), and the difference $\Delta\tilde{v}_{\rm los}$ between $\tilde{v}_{\rm los}$ in the BS2 and B simulations. To make more realistic the comparison with, e.g. WEAVE[4], we consider only those particles with Galactic latitude $|b - 2^\circ| < 1^\circ$. Moreover, the distance of the particles d is then convolved with random errors drawn from Gaussian distributions with standard deviation $0.1d$, in order to simulate the typical error of the photometric distance estimate of the red clump stars (see Monari et al. 2014).

We see from these plots how an accurate choice of the lines-of-sight of the spectroscopic survey would allow to disentangle between different models of the Milky Way, as the signal in $\tilde{v}_{\rm los}$ is significant at distances between 1 and 6 kpc from the Sun, with peak signals of $\sim \pm 15$ km s^{-1}, in the cases with the bar. The distance error does not blur the signal, and the differences between the different models remain recognizable.

In particular, from the bottom right panel of Fig. 12 we see that the difference between the BS2 and B models reaches amplitudes of $\sim 6-9$ km s^{-1}, larger than the typical error in $\tilde{v}_{\rm los}$ of a survey like WEAVE, hence allowing to disentangle bar-only models from models including both a bar and spiral arms. Even though these differences are relatively small, more generally speaking the non-linear enhancement of the mean vertical velocities in the presence of spiral arms compared to a bar-only case is a major feature that will allow in the future to disentangle the respective contribution of the bar and spirals to the Galactic potential. Indeed, no realistic parameters in a bar-only model could ever reproduce the vertical mean motions produced in the BS2 model, without causing much larger and unrealistic radial motions (see M15). Hence, the bar-only models and bar+spiral models are not degenerate with each other as long as one considers both the radial and vertical mean motions. However, in reality the matters are complicated further by the possible influence of external perturbers on the dynamics of the outer disc (but probably not that much in the inner disc).

7 DISCUSSION AND CONCLUSIONS

In this work, by means of three-dimensional test-particle numerical simulations, we have focused on the kinematics of the stars of the Galactic disc when it is affected by the coupled gravitational perturbations of a bar and quasi-static spiral arms of different pattern speeds.

While these effects are essentially the sum of the effects of the single perturbers for in-plane motions away from major resonances, our major finding is that significant non-linear motions appear from the coupling in the vertical kinematics *everywhere* in the disc. These effects are able to double the amplitude of the vertical breathing modes generated by spirals alone. In particular, there seems to be an increase of the 'compression' (i.e. of the number of stars with velocity pointing towards the Galactic plane) on the top of the arms and of the 'rarefaction' (i.e. of the number of stars moving away from the plane) in the interarm regions.

Looking at the power spectrum of the peculiar line-of-sight velocity, like in the recent work of Bovy et al. (2015), does not make these non-linear effects appear because this method makes use only of the component of the velocity parallel to the Galactic plane. If confirmed by further surveys, the large-scale velocity fluctuations observed with APOGEE are thus indeed predominantly affected by the Galactic bar, provided the bar is strong enough. But the amplitude of spi-

[4] Note that since WEAVE is a survey of the Northern sky, and only the Galactic longitudes ranging from $l \simeq 20^\circ$ to $l \simeq 225^\circ$ will be observed.

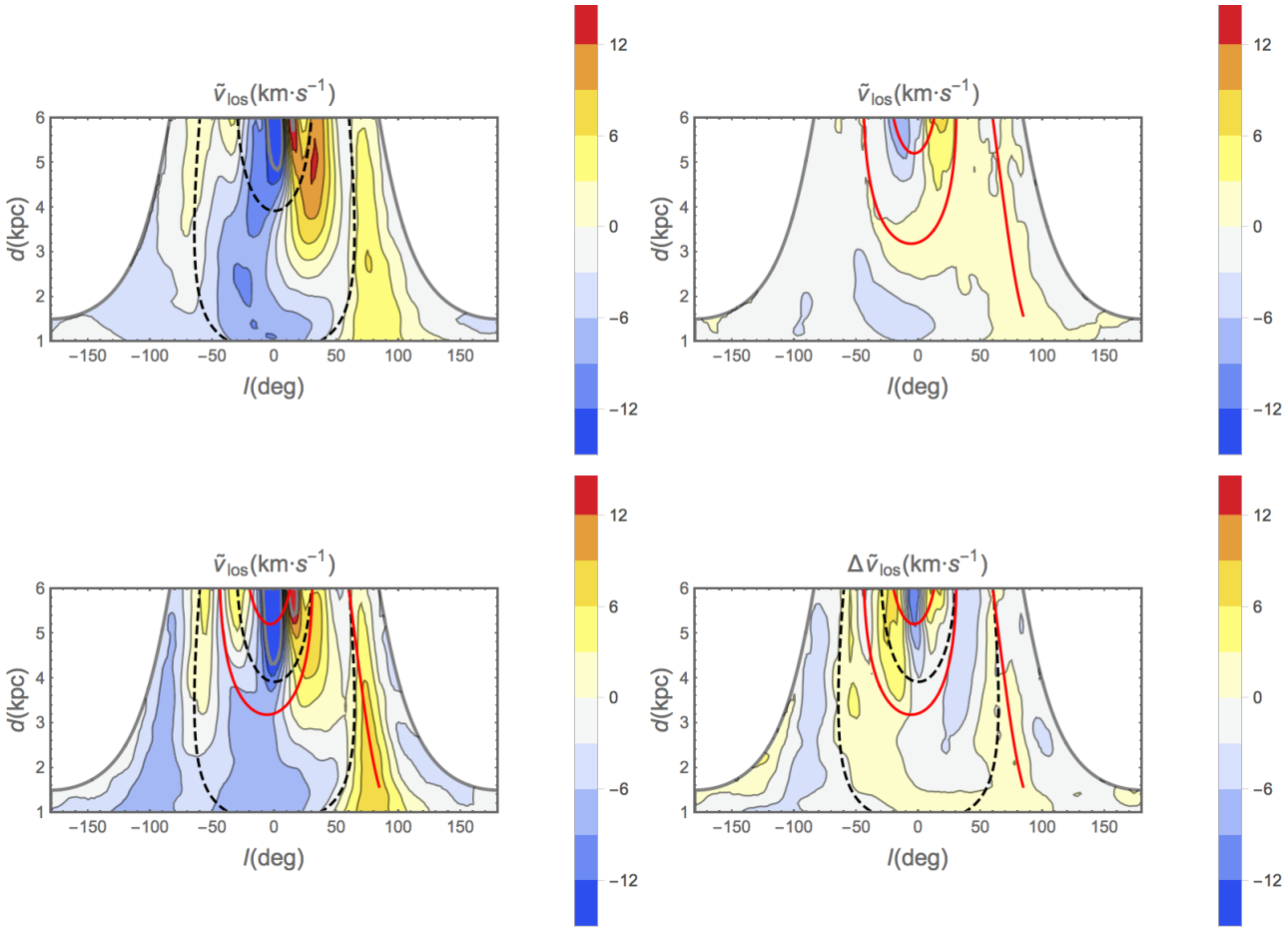

Figure 12. Peculiar velocity as a function of the Galactic longitude l, and distance d from the Sun, computed for some simulations presented in this work. Top left panel: $\tilde{v}_{\rm los}$ for the B simulation. Top right panel: $\tilde{v}_{\rm los}$ for the S2 simulation. Bottom left panel: $\tilde{v}_{\rm los}$ for the BS2 simulation. Bottom right panel: $\Delta\tilde{v}_{\rm los}$, obtained subtracting $\tilde{v}_{\rm los}$ for BS2 and $\tilde{v}_{\rm los}$ for B. The particles used to compute these plots have $|b - 2^\circ| < 1^\circ$. The black dashed curves represent the corotation and the outer Lindblad resonance of the bar, the red curves the loci of the spiral arms.

rals certainly does not have to be negligible for the power spectrum to match APOGEE observations. In order to make use of the noticeable differences in terms of vertical motions, we have shown how it will be possible for a spectroscopic survey like WEAVE alone to distinguish between bar-only and bar+spiral models. The way to do this is to use the true (and not projected) line-of-sight velocity, to have fields of view slightly inclined with respect to the Galactic plane, and distributed rather continuously in Galactic longitudes, like it was suggested also by Kawata et al. (2014); Hunt et al. (2015). The typical distance error expected for red clump giants does not blur the signal of the different models. Note that the differences are not solely due to differences in $\langle v_z \rangle$, but also in $\langle v_\phi \rangle$ and $\langle v_R \rangle$.

Finally, in agreement with previous two-dimensional investigations (Minchev & Famaey 2010), we confirmed that the coupling of the bar and spiral arms enhances the radial migration even when the spiral amplitude is non-varying, and even when low-order spiral resonances overlap with the bar. We found a significant fraction of orbits crossing the OLR of the bar. This means that the OLR is not a barrier separating the chemical evolution and churning of the inner disc from the outer disc (Halle et al. 2015), although in the absence of significant spiral arms, stars from the inner disc do not migrate to the outer disc.

In conclusion, the non-linear effects due to the coupling of a bar and spiral arms of different pattern speeds are significant, and have to be taken in consideration in future models of the Galaxy. To do this, theoretical insight of the problem is necessary, in the spirit of M16, but with two perturbers instead of one, which will be the topic of a follow-up paper.

ACKNOWLEDGMENTS

We thank the anonymous referee for insightful comments on this manuscript and Jo Bovy for useful discussions. This work has been supported by a postdoctoral grant from the *Centre National d'Etudes Spatiales* (CNES) for GM. RG acknowledges support through the DFG Research Centre SFB-881 'The Milky Way System' through project A1.

REFERENCES

Antoja T., Figueras F., Romero-Gómez M., Pichardo B., Valenzuela O., Moreno E., 2011, MNRAS, 418, 1423
Antoja T. et al., 2014, A&A, 563, A60
Antoja T., Roca-Fabrega S., de Bruijne J., Prusti T., 2016, arXiv:1602.07687
Baba J., Saitoh T. R., Wada K., 2013, ApJ, 763, 46
Benjamin R. A. et al., 2005, ApJ, 630, L149
Bienayme O., Sechaud N., 1997, A&A, 323, 781
Binney J., Tremaine S., 2008, Galactic Dynamics: Second Edition, Binney, J. & Tremaine, S., ed. Princeton University Press
Bovy J., Bird J. C., García Pérez A. E., Majewski S. R., Nidever D. L., Zasowski G., 2015, ApJ, 800, 83
Carlin J. L. et al., 2013, ApJ, 777, L5
Ceverino D., Klypin A., 2007, MNRAS, 379, 1155
Chereul E., Creze M., Bienayme O., 1998, A&A, 340, 384
Chirikov B. V., 1979, Phys. Rep., 52, 263
Churchwell E. et al., 2009, PASP, 121, 213
Content D. et al., 2013, in Proc. SPIE, Vol. 8860, UV/Optical/IR Space Telescopes and Instruments: Innovative Technologies and Concepts VI, p. 88600E
Cox D. P., Gómez G. C., 2002, ApJS, 142, 261
Dalton G. et al., 2012, in Proc. SPIE, Vol. 8446, Ground-based and Airborne Instrumentation for Astronomy IV, p. 84460P
Debattista V. P., 2014, MNRAS, 443, L1
Dehnen W., 1998, AJ, 115, 2384
Dehnen W., 1999, ApJ, 524, L35
Dehnen W., 2000, AJ, 119, 800
D'Onghia E., Vogelsberger M., Hernquist L., 2013, ApJ, 766, 34
Famaey B., Jorissen A., Luri X., Mayor M., Udry S., Dejonghe H., Turon C., 2005, A&A, 430, 165
Faure C., Siebert A., Famaey B., 2014, MNRAS, 440, 2564
Gómez F. A., White S. D. M., Marinacci F., Slater C. T., Grand R. J. J., Springel V., Pakmor R., 2016, MNRAS, 456, 2779
Gouda N. et al., 2006, in Proc. SPIE, Vol. 6265, Society of Photo-Optical Instrumentation Engineers (SPIE) Conference Series, p. 626542
Grand R. J. J., Bovy J., Kawata D., Hunt J. A. S., Famaey B., Siebert A., Monari G., Cropper M., 2015a, MNRAS, 453, 1867
Grand R. J. J., Kawata D., Cropper M., 2012, MNRAS, 426, 167
Grand R. J. J., Springel V., Gómez F. A., Marinacci F., Pakmor R., Campbell D. J. R., Jenkins A., 2015b, arXiv: 1512.02219
Halle A., Di Matteo P., Haywood M., Combes F., 2015, A&A, 578, A58
Haywood M., Lehnert M. D., Di Matteo P., Snaith O., Schultheis M., Katz D., Gomez A., 2016, arXiv:1601.03042
Hunt J. A. S., Kawata D., Grand R. J. J., Minchev I., Pasetto S., Cropper M., 2015, MNRAS, 450, 2132
Kawata D., Hunt J. A. S., Grand R. J. J., Pasetto S., Cropper M., 2014, MNRAS, 443, 2757
Kubryk M., Prantzos N., Athanassoula E., 2015, A&A, 580, A126
Kuijken K., Tremaine S., 1991, in Dynamics of Disc Galaxies, Sundelius B., ed., p. 71
Lin C. C., Shu F. H., 1964, ApJ, 140, 646
Lin C. C., Shu F. H., 1966, Proceedings of the National Academy of Science, 55, 229
Majewski S. R. et al., 2015, arXiv:1509.05420
Minchev I., Chiappini C., Martig M., 2013, A&A, 558, A9
Minchev I., Famaey B., 2010, ApJ, 722, 112
Minchev I., Famaey B., Quillen A. C., Di Matteo P., Combes F., Vlajić M., Erwin P., Bland-Hawthorn J., 2012, A&A, 548, A126
Monari G., Antoja T., Helmi A., 2013, arXiv:1306.2632
Monari G., Famaey B., Siebert A., 2015, MNRAS, 452, 747
Monari G., Famaey B., Siebert A., 2016, MNRAS, 457, 2569
Monari G., Helmi A., Antoja T., Steinmetz M., 2014, A&A, 569, A69
Mühlbauer G., Dehnen W., 2003, A&A, 401, 975
Pompéia L. et al., 2011, MNRAS, 415, 1138
Portail M., Wegg C., Gerhard O., Martinez-Valpuesta I., 2015, MNRAS, 448, 713
Quillen A. C., Dougherty J., Bagley M. B., Minchev I., Comparetta J., 2011, MNRAS, 417, 762
Quillen A. C., Minchev I., 2005, AJ, 130, 576
Romero-Gómez M., Athanassoula E., Masdemont J. J., García-Gómez C., 2007, A&A, 472, 63
Sellwood J. A., Binney J. J., 2002, MNRAS, 336, 785
Sellwood J. A., Carlberg R. G., 2014, ApJ, 785, 137
Shu F. H., 1969, ApJ, 158, 505
Siebert A. et al., 2012, MNRAS, 425, 2335
Siebert A. et al., 2011, MNRAS, 412, 2026
Sormani M. C., Binney J., Magorrian J., 2015, MNRAS, 449, 2421
Spergel D. N. et al., 2009, in Bulletin of the American Astronomical Society, Vol. 41, American Astronomical Society Meeting Abstracts #213, p. 362
Wegg C., Gerhard O., Portail M., 2015, MNRAS, 450, 4050
Weinberg M. D., 1994, ApJ, 420, 597
Widrow L. M., Gardner S., Yanny B., Dodelson S., Chen H.-Y., 2012, ApJ, 750, L41
Williams M. E. K. et al., 2013, MNRAS, 436, 101